How to cite: Angew. Chem. Int. Ed. 2023, e202301176
doi.org/10.1002/anie.202301176

Thermoelectric Materials

Investigating the Role of Vacancies on the Thermoelectric Properties of EuCuSb-Eu_2ZnSb_2 Alloys

*Sevan Chanakian, Wanyue Peng, Vanessa Meschke, A. K. M. Ashiquzzaman Shawon, Jesse Adamczyk, Valeri Petkov, Eric Toberer, and Alexandra Zevalkink**

Abstract: *AMX* compounds with the ZrBeSi structure tolerate a vacancy concentration of up to 50 % on the *M*-site in the planar *MX*-layers. Here, we investigate the impact of vacancies on the thermal and electronic properties across the full $EuCu_{1-x}Zn_{0.5x}Sb$ solid solution. The transition from a fully-occupied honeycomb layer (EuCuSb) to one with a quarter of the atoms missing ($EuZn_{0.5}Sb$) leads to non-linear bond expansion in the honeycomb layer, increasing atomic displacement parameters on the *M* and Sb-sites, and significant lattice softening. This, combined with a rapid increase in point defect scattering, causes the lattice thermal conductivity to decrease from 3 to 0.5 $W\,mK^{-1}$ at 300 K. The effect of vacancies on the electronic properties is more nuanced; we see a small increase in effective mass, large increase in band gap, and decrease in carrier concentration. Ultimately, the maximum zT increases from 0.09 to 0.7 as we go from EuCuSb to $EuZn_{0.5}Sb$.

Introduction

Since the discovery of thermoelectricity by Alessandro Volta in 1794, scientists have been investigating thermoelectric materials to understand the complex interplay between electronic and thermal transport.[1,2] Promising thermoelectric materials exhibit a large power factor, ($\frac{\alpha^2}{\rho}$ where α is the Seebeck coefficient and ρ is the electrical resistivity), and low thermal conductivity, κ. These criteria are encompassed by the thermoelectric figure of merit, $zT = \frac{\alpha^2 T}{\rho\kappa}$. One of the most widely successful approaches to improve zT is to reduce the lattice (phonon) contribution (κ_L) to the thermal conductivity by designing materials with low speed of sound (v) or short phonon relaxation times (τ). Various techniques to scatter and/or reduce phonon velocities have been identified, including: alloying, nano-structuring, introducing structural disorder and anharmonicity, and leveraging structural complexity.[3–7]

Compounds with the ZrBeSi-structure can form with a wide range of compositions and can incorporate large defect concentrations, making it a ripe space to explore structure–property relationships.[8] The ZrBeSi structure (space group $P6_3/mmc$) is a ternary derivative of AlB_2 (space group $P6/mmm$), in which the Be and Si form a planar anionic hexagonal net (i.e., honeycomb layer).[9] The Zr cations reside in 12-fold coordinated hexagonal prisms in between the anionic layers. Recent studies have highlighted features of the ZrBeSi-structure that allow for exceptionally low thermal conductivity, while simultaneously maintaining high mobility ($>100\,cm^2V^{-1}s^{-1}$).[10–14] Computational work has shown that strong out-of-plane vibrations of the honeycomb layers composing the ZrBeSi-structure can lead to large anharmonicity, which contributes to the low thermal conductivity in materials of this structure type.[10,11,15] Additionally, several compounds in the ZrBeSi structure type have been identified as having low thermal conductivity thanks to their heavy atoms and soft bonds.[11,14–18] Notable compounds within this class that are of interest for thermoelectrics include LaPbSb with a $zT \approx 0.26$ at 300 K, SrAgSb with a $zT \approx 0.6$ at 773 K, and BaAgSb with a $zT \approx 0.73$ at 773 K.[13,14,17]

The most remarkable aspect of the ZrBeSi structure is its ability to accommodate 50 % vacancies on the metal-site, as illustrated in Figure 1a and d. This was first noted by Wilson et al. with the discovery of A_2ZnPn_2 (A = Sr, Eu and Pn = As, Sb).[19,20] A_2ZnPn_2 can alternatively be written as $AZn_{0.5}Pn$, a convention that we will use henceforth, in keeping with the *AMX* stoichiometry of the parent ZrBeSi-structure type. The high vacancy concentration and resulting local distortions have been identified as a root cause for the ultralow thermal conductivity in $EuZn_{0.5}Sb$ ($0.55\,W\,mK^{-1}$).[12,21–23] $EuZn_{0.5}Sb$ has been of particular interest for its high performance as a thermoelectric ($zT \approx 1.0$ at 823 K) and its capacity for topological electronic structure transitions.[22,24] In the average $EuZn_{0.5}Sb$ structure, the Zn vacancies are randomly distributed on the Zn site in

[*] S. Chanakian, W. Peng, A. K. M. Ashiquzzaman Shawon, A. Zevalkink
Department of Chemical Engineering and Materials Science, Michigan State University, East Lansing MI 48824 (USA)
E-mail: alexzev@msu.edu
V. Meschke, J. Adamczyk, E. Toberer
Department of Physics, Colorado School of Mines, Golden, CO 80401 (USA)
V. Petkov
Department of Physics, Central Michigan University, Mt. Pleasant, MI 48858 (USA)

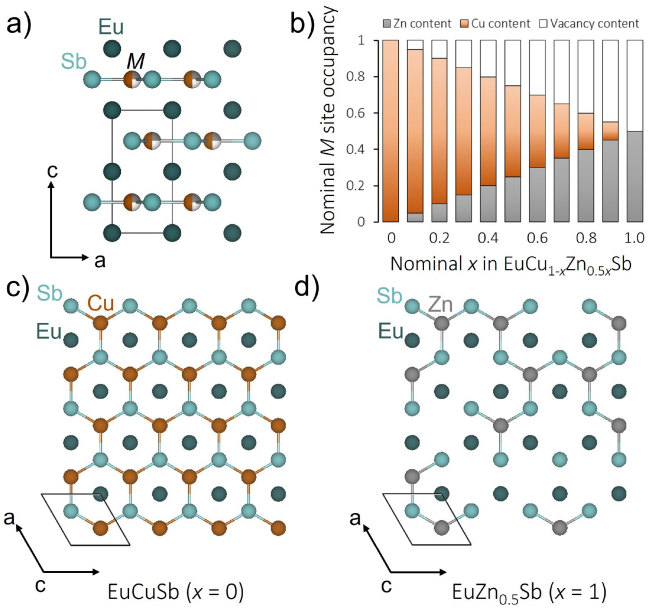

Figure 1. a) The average structure of $EuCu_{1-x}Zn_{0.5x}Sb$ is a defect variant of the ZrBeSi-structure type. b) A visual illustration of the relative Cu, Zn, and vacancy concentrations of the *M*-site in the $EuCu_{1-x}Zn_{0.5x}Sb$ series. c) An illustration of the fully-filled hexagonal net found in EuCuSb and d) the deconstructed net that results when 50% of the *M*-atoms are removed, as is the case for $EuZn_{0.5}Sb$.

the structure (i.e., there is no long-range order).[19] However, a recent computational study supported by high-angle annular dark-field scanning transmission electron microscopy (HAADF-STEM) suggests that short-range ordering of vacancies leads to local, nano-scale domains characterized by staggered rows of Zn vacancies.[24] The same study showed that the size of the band gap of $EuZn_{0.5}Sb$ is highly sensitive to vacancy ordering. The local ordering of Zn and vacancies on the *M*-site in $EuZn_{0.5}Sb$ is thought to induce intrinsic nano-structuring of crystallites, which contribute to phonon-scattering.[21]

Despite the importance of vacancies in controlling the properties of the $AZn_{0.5}Pn$ family of materials, there have been limited studies on the effects of varying the vacancy concentration on the structure and thermoelectric properties.[23,25] For example, the vacancy concentration in $EuZn_{0.5}Sb$ was tuned within a narrow range via substitution of 2% of Ag on the Zn-site, leading to a zT of $\approx$1.1 at 823 K.[23] However, there is no prior work investigating the full range from 0 to 50% vacancy concentration on the Zn-site. In this work, we investigate the solid solution between $EuZn_{0.5}Sb$ and EuCuSb. The latter compound, EuCuSb, has garnered interest in the thermoelectric community and has also been identified as a frustrated magnet.[14,26] We demonstrate that a complete solid solution forms between the fully-filled and half-filled ZrBeSi-structures, which we represent as $EuCu_{1-x}Zn_{0.5x}Sb$ ($0 \le x \le 1$). The nominal Cu, Zn and vacancy occupation on the metal site is illustrated in Figure 1b. Since Cu has a 1+ charge and Zn has a 2+ charge, the system remains (nominally) valence precise across the full solid solution. Furthermore, the similar ionic radii and mass of Zn^{2+} and Cu^{1+} make this an ideal solid-solution with which to study the impact of vacancy concentration on transport properties. We proceed to investigate the structural, thermal, and electronic properties of the series to unearth the fundamental physical phenomena derived from vacancies in the structure.

Results and Discussion

Trends in structure and bonding

The $EuCu_{1-x}Zn_{0.5x}Sb$ series adheres to the Zintl-Klemm formalism of charge counting i.e., $Eu^{2+}[Cu^{1+}Sb^{3-}]^{2-}$ and $[Eu_2^{2+}]^{4+}[Zn^{2+}Sb_2^{3-}]^{4-}$. Thus, to maintain charge neutrality, it is necessary to remove two Cu-atoms for every Zn substituted onto the lattice. As a consequence, the honeycomb layers evolve to form a discontinuous mixture of ribbons and moieties. This is illustrated in Figure 1c and d. Our efforts to understand the implications of these drastic changes begin with an analysis of the X-ray diffraction (XRD) patterns. XRD confirms the successful synthesis of all compounds: $EuCu_{1-x}Zn_{0.5x}Sb$ ($0 \le x \le 1$) (Figure S1). A careful Rietveld refinement of the XRD patterns was conducted to confirm the compositions of the samples and to experimentally refine the occupancies of the Zn, Cu, and Sb, in turn quantifying the vacancy concentrations. The results of these refinements along with the compositions determined by energy dispersive spectroscopy (EDS) are presented in Table S1 of the Supporting Information. While the results of the experimentally quantified vacancy concentrations are consistent with the nominal stoichiometry, innate uncertainties of the experimental techniques used result in less than clear interpretation of the materials properties. For this reason, all trends in the remainder of this article are modeled as a function of nominal composition. The lattice parameters (Figure 2), determined from Rietveld refinement, reveal an increase in the *a*-parameter as Zn and vacancies are substituted onto the *M*-site. This expansion implies that increasing the vacancy concentration leads to an increase in the average *M*-Sb bond lengths. While this result may seem unintuitive, similar lattice expansion due to cation vacancies has been observed in other structure types and has been attributed to anion-anion repulsion.[28] While the *a*–*b* plane expands with increasing vacancies, the *c*-parameter contracts (Figure 2b), thus shortening the distance between the *M*-Sb honeycombs and Eu-cation sheets. The simultaneous expansion in the *a*-direction and contraction in the *c*-direction results in an incremental increase in volume.

Curiously, these changes to the unit cell parameters are not linear as a function of x ($EuCu_{1-x}Zn_{0.5x}Sb$). Instead, the lattice parameters vary as a function of $\frac{x}{(2-x)}$, which we interpret as the ratio of vacant to filled *M*-sites (regardless of whether Cu or Zn occupies the site). This can be described by the following expressions, which are plotted (dashed lines) in Figure 2.

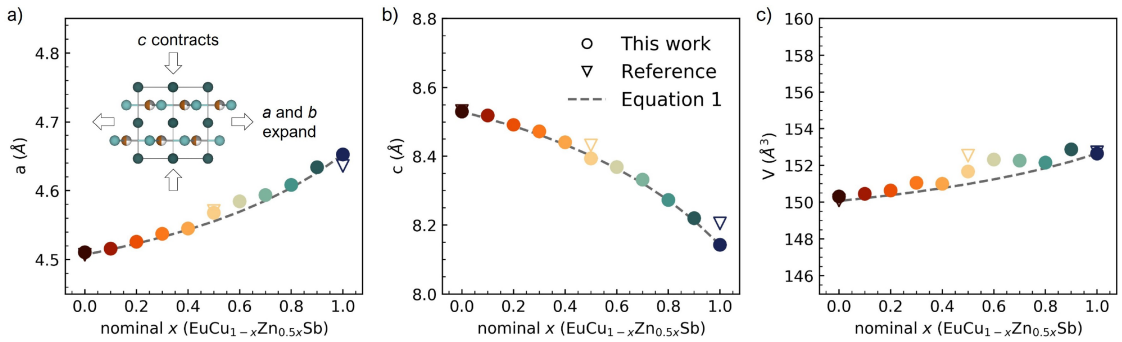

Figure 2. The lattice parameters *a* and *c* and the unit cell volume, *V*, of $EuCu_{1-x}Zn_{0.5x}Sb$ are shown as a function of increasing *x* corresponding to increasing vacancy concentration. The *a* and *c* parameters experience significant non-linear expansion and contraction, respectively, resulting in a moderate expansion of the volume. Reference data taken from Refs. [19,25,27]. The dashed line described by Equation 1 models the importance of vacancies in this structure.

$$a_x = a_{x=0} + \frac{(x)}{(2-x)}(a_{x=0} - a_{x=1}),$$
$$c_x = c_{x=0} + \frac{(x)}{(2-x)}(c_{x=0} - c_{x=1}) \quad (1)$$

The excellent fit to the observed lattice parameter trends suggests that the vacancy concentration, not the Cu:Zn ratio, controls the structure.

In our discussion up until now, we have assumed that the anionic honeycomb layers are planar (i.e., maintain the ZrBeSi structure type) for *x* ranging from 0 to 1. We began with this assumption because both EuCuSb and $EuZn_{0.5}Sb$ were reported to have flat anionic layers based on single crystal diffraction.[19,27] However, Zhang et al. showed that the honeycomb layers in samples of $EuCu_{0.5}Zn_{0.25}Sb$ exhibit a slight corrugation of 0.07° degrees[25] resulting in a LiGaGe-type structure. This raises the question of whether there is corrugation of the honeycomb layers for intermediate values of *x*. In the current study, we used pair distribution function (PDF) analysis of samples with $x=0.3$ and $x=0.7$ to probe the local structure, looking for evidence of corrugation or other deviations for the nominal ZrBeSi structure type. We first fit the data using the average ZrBeSi structure which modeled the experimental data reasonably well (i.e., $R_w=0.0991$ for $x=0.3$ and $R_w=0.1198$ for $x=0.7$). We tested the corrugated model proposed by Zhang et al.,[25] but it did not improve the fit to the PDF data (see S3). Ultimately, we do not observe clear evidence of corrugation in our Rietveld analysis or in our PDF analysis. However, we did observe large atomic displacements (ADP) that might be consistent with locally corrugated hexagonal nets. The ADP illustrated by the isosurfaces in Figure 3b and d suggest the Sb and *M*-species have freedom to move in the *z*-direction. It should be noted that while the *z*-displacement on the *M*-site is consistently highest for $x=0.7$, the $x=0.3$ sample can be modeled equally well with large *z*-displacement on either the Sb or the *M*-site (see Figure S4). For consistency, we have presented the solution with larger *z*-displacement on the *M*-site for both compositions in Figure 3.

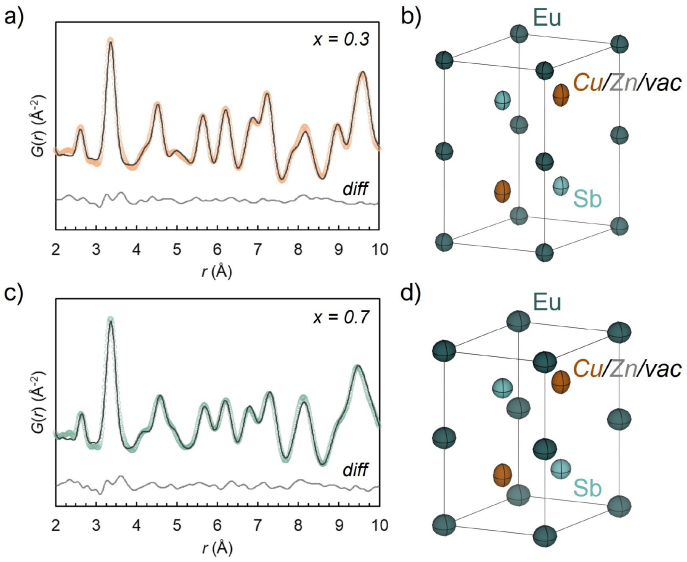

Figure 3. PDF results of the $EuCu_{1-x}Zn_{0.5x}Sb$ a) $x=0.3$ and c) $x=0.7$ indicate the ZrBeSi-structure is a reasonable model for the average structure. Large displacement on the *M*-site along the *z*-direction for b) $x=0.3$ and d) $x=0.7$, illustrated by the ADP ellipsoids, is suggestive of local buckling of the honeycombs.

A comparison of the ADP ellipsoids for $x=0.3$ and $x=0.7$ illustrates the general increase in atomic displacement of all atoms with increasing *x*. The change is particularly evident on the *M*-site, which exhibits the greatest increase in displacive freedom. This observation is evidence of the considerable disorder caused by the vacancies in the $EuCu_{1-x}Zn_{0.5x}Sb$ material system. Large ADP values are also consistent with the presence of negative chemical pressure[29] in this system, a feature that is likely further enhanced by high vacancy concentrations. Although we modeled the PDF data using the nominal ZrBeSi structure, it is still possible that various energetically-degenerate schemes for vacancy ordering and corrugation of the hexagonal net compete in this system, each existing in nano-sized domains within the polycrystalline samples. This would lead to a sample that still appears to have the average

structure and would explain the high ADP values observed in PDF.

Whether or not local ordering is present in the structure, it remains clear that the average bond length (and unit cell volume) increases as a function of increasing x. In general, compounds become softer (smaller elastic moduli) as bond lengths increase, as described by the Lennard–Jones Potential.[30] To verify this experimentally, we use resonant ultrasound spectroscopy to probe the elastic moduli of the $EuCu_{1-x}Zn_{0.5x}Sb$ series. As shown in Figure 4a), the transition from fully-filled EuCuSb to vacancy-rich $EuZn_{0.5}Sb$ results in a ≈30 % decrease in the Young's, bulk and shear moduli, which is much greater than one might expect from the ≈2 % increase in unit cell volume. This softening is in part due to the addition of vacancies which serve to destabilize the otherwise stiff, covalent M-Sb hexagonal network. Additionally, we note that in general Zn–Sb compounds are softer than Cu–Sb based materials. A survey of all Zn–Sb and Cu–Sb binary compounds reported in MaterialsProject.org reveals that, on average, Zn-containing antimonides have nearly 50 % lower stiffness (see Table S4).[31] Note, however, that Table S4 is a not a comparison of isostructural compounds, so other factors may be at play. This tendency towards softer bonds in Zn-based antimonides may be related to the lower Pauling bond disassociation energy of Zn–Sb bonds (1.18 eV) compared with Cu–Sb bonds (2.59 eV). While the elastic moduli quantify the stiffness of bonds, the bond dissociation energy is a metric of bond strength. Although the bond stiffness and bond strength are rooted in different features of an atomic bond (i.e., curvature vs. depth of Lenard-Jones potential well, respectively), it has been proposed that these parameters are directly correlated.[32,33] Finally, Figure 4b) shows the temperature dependence of the Young's modulus of EuCuSb and $EuZn_{0.5}Sb$. This trend also holds for the bulk and shear moduli which are shown in Figure S5. Surprisingly, even though EuCuSb has stiffer bonds than $EuZn_{0.5}Sb$ at room temperature, the former compound softens more rapidly with increasing temperature. The potential implications of the higher softening rate, as it relates to the anharmonicity of the material, are discussed in Isotta et al. 2022.[34]

Thermoelectric properties

Figure 5 shows the temperature-dependent thermoelectric properties for the $EuCu_{1-x}Zn_{0.5x}Sb$ series. The positive Seebeck coefficients (α) confirm all samples are p-type semiconductors, consistent with their respective Hall carrier concentrations (n_H, Figure 6a). The moderately positive slope of the resistivity (ρ) over the measured temperature range is evidence of the degenerate semiconducting nature of all samples in the $EuCu_{1-x}Zn_{0.5x}Sb$ series. As a general trend, both ρ and α increase as we increase x, despite the charge-neutral nature of all nominal compositions. These increases are accounted for by the general decrease in the hole-dominated n_H (Figure 6a). In Zn-rich samples ($x > 0.4$), the maxima in the Seebeck coefficient near 675 K suggest the onset minority carrier activation and bipolar transport. A detailed analysis and discussion of the composition-dependence of the band gap, carrier mobility and effective mass, is presented in Section "Composition dependent electronic properties", below.

The total thermal conductivity (κ_{Total}) consists of contributions from various sources, most prominently the electronic (κ_e) and lattice (κ_L) components (i.e., $\kappa_{Total} = \kappa_e + \kappa_L$). Here, $\kappa_e = LT/\rho$, where L is the Lorenz number determined from α as described in Kim et al..[3] A large reduction in κ_{Total} is observed with increasing x, due to a simultaneous reduction in both κ_e and κ_L contributions. As the vacancy concentration increases in the $EuCu_{1-x}Zn_{0.5x}Sb$ series, the κ_L vs. temperature curves begin to flatten. Flat trends in temperature-dependent κ_L indicates grain-boundary and point-defect phonon scattering.[35] All samples were synthesized using similar processing to control for grain-size, however there is variation between samples as indicated by the scanning electron microscopy (SEM) images of fracture surfaces in Figure S2. It is observed that the sample with the largest average grain size is the sample with the highest number of vacancies, i.e., $x = 1$. Thus, we attribute the

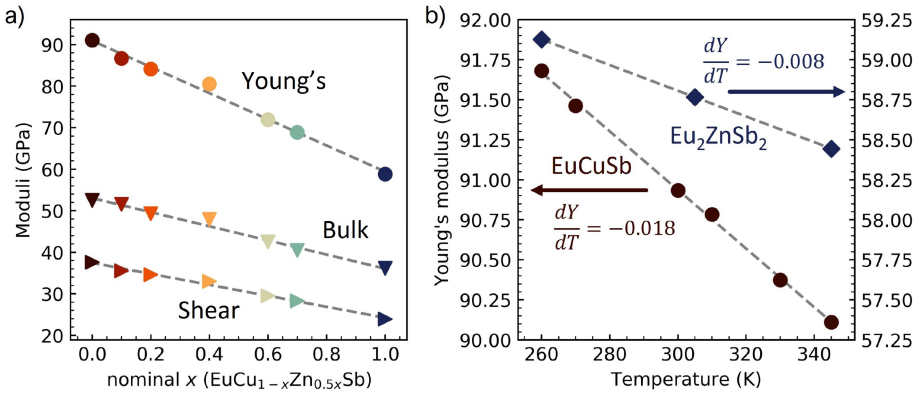

Figure 4. a) The Young's, bulk and shear moduli of $EuCu_{1-x}Zn_{0.5x}Sb$ samples are found to soften linearly with respect to x. b) Temperature-dependent Young's moduli of the end-compounds indicate higher anharmonicity in EuCuSb.

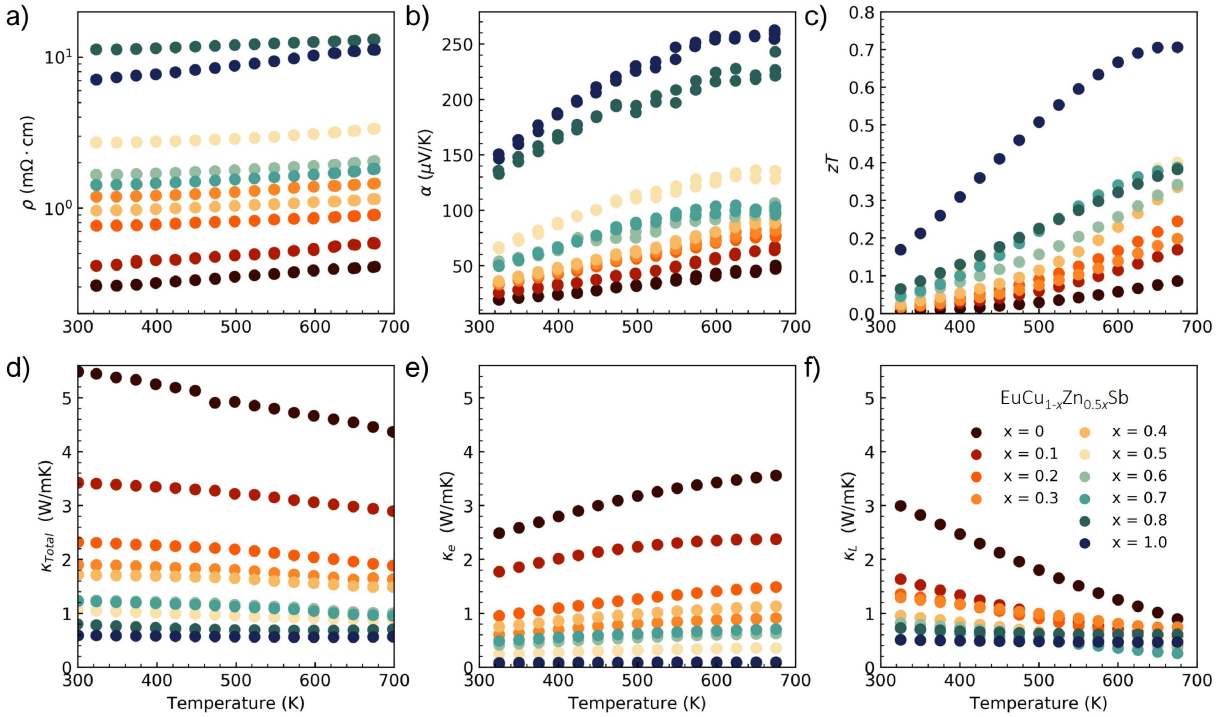

Figure 5. The temperature-dependent transport properties of the $EuCu_{1-x}Zn_{0.5x}Sb$ series are shown. The top panels show a) resistivity, ρ, b) Seebeck coefficient, α, and c) figure of merit, zT. The bottom panels show d) total thermal conductivity, κ_{Total}, e) electronic thermal conductivity, κ_e, and f) lattice thermal conductivity, κ_L. Ultimately, an 8-fold increase in zT is observed for the fully-Zn substituted sample, $x=1$, due to increased α and decreased κ_{Total} with increasing x. The temperature-independent κ_L in samples with $x>0.7$ suggests point-defect scattering limits phonon transport, which is consistent with the increased vacancy concentrations.

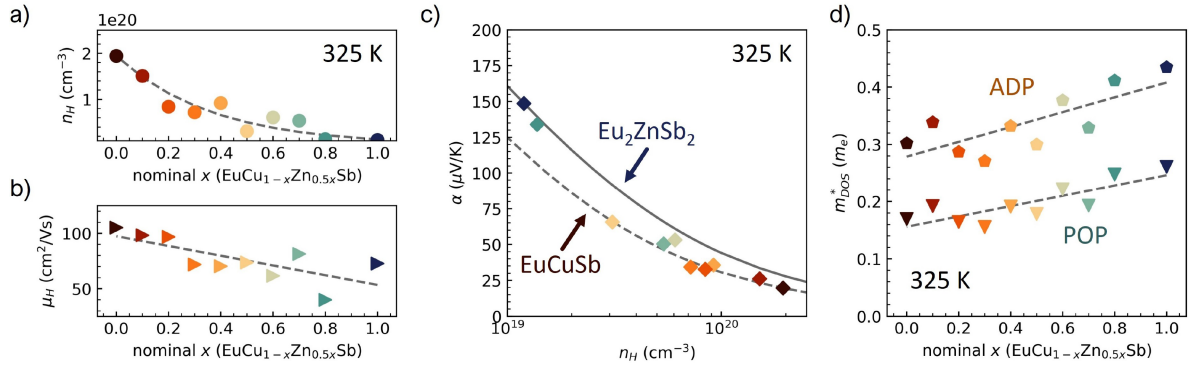

Figure 6. a) Composition-dependent n_H and b) composition-dependent μ_H at 325 K. c) The Seebeck Pisarenko curves generated by the SPB model of EuCuSb (solid line) and Eu_2ZnSb_2 (dashed line), along with the experimental data for the full $EuCu_{1-x}Zn_{0.5x}Sb$ solid solution. d) The DOS effective mass as a function of composition assuming ADP (pentagons) and POP (triangles) scattering. Both estimates of m^*_{DOS} show moderate increase over the range in composition.

flattening slope in this system to increased phonon scattering by point-defects (i.e., vacancies). That is to say, the flattening slope with increasing x reflects a shift from Umklapp-dominated phonon scattering in EuCuSb ($x=0$) to defect-dominated scattering when in $EuZn_{0.5}Sb$ ($x=1$). A discussion of the composition-dependent sound velocity and phonon scattering rates can be found in Section "Composition dependent thermal properties".

The temperature-dependent zT indicates a steady increase in efficiency with temperature for all samples. A maximum zT of 0.71 at 675 K is attained in the $EuZn_{0.5}Sb$ end-member, which is comparable to previous reports of zT for this compound.[12,22] The zT increases by more than a factor of 8 at 675 K as the composition changes from $x=0$ to $x=1$. This is due to the simultaneous increase in α and decrease in κ_{Total}. The electrical resistivity ultimately limits the zT for the $x=1$ sample. While the alloyed compositions ($0<x<1$) do exhibit a reduced κ_{Total} when compared to $x=0$ and a reduced ρ when compared to $x=1$, their zT values do not surpass that of $x=1$ due to a reduction in α. It should be

noted that n_H of the compounds in this series have not been optimized for maximum zT (see Figure S9). By tuning n_H, a higher α and therefore a higher zT can be expected, however this is outside the scope of this work. Instead, we look to understand the complex interplay of electronic and thermal properties with respect to the vacancy concentration which warrants a deeper dive.

Composition dependent electronic properties

Figure 6a and b show the change in room-temperature Hall carrier concentration (n_H) and Hall mobility (μ_H) as a function of x. Polynomial-fits to the temperature-dependent Hall data (see Figure S8) were used to determine the values of n_H and μ_H at 325 K (see Figure 6), thus enabling us to identify isothermal trends in composition. Small deviations in the occupancy of the M-site and potentially the presence of cation vacancies contribute to large variation in n_H.[22,23] These deviations originate in the unavoidable uncertainties associated with synthesis (e.g., weighing elements, ball milling, SPS). Thus the composition-dependent electronic properties deviate from monotonically trending. Regardless, we can discern overall trends in the composition dependence of n_H and μ_H for this solid solution. With the addition of Zn and vacancies into the EuCuSb structure, n_H exhibits an order of magnitude decrease (i.e. 2×10^{20} for $x=0$ vs. 10^{19} for $x=1$)—despite the overall charge neutral stoichiometries of the nominal compositions. Simultaneously, we observe a decrease in μ_H with increasing x. The minimum μ_H is found in the most vacancy-rich samples, suggesting that defect scattering is, as one would expect, the dominant factor limiting the mobility of these compounds. However, to explore additional factors that might play a role in the mobility trends, we probe the x-dependent experimental band gap, E_g, and the density of states effective mass, m^*_{DOS}.

While the Seebeck coefficient does not exhibit a maxima for all compositions (i.e., $x\leq0.7$), we can approximate the Goldsmid-Sharp bang-gap, $E_g \approx 2eT_{max}|\alpha_{max}|$, for the $x=0.8$ ($E_g\approx0.31$ eV) and $x=1$ ($E_g\approx0.35$ eV) samples.[36] The band gap for the $x=1$ sample is consistent with previous reports of $EuZn_{0.5}Sb$ ($E_g\approx0.34$ eV).[12] A comparison of the optical E_g for $EuZn_{0.5}Sb$ ($E_{g,opt}\approx0.25$ eV for sample with $n_H\approx10^{19}$ cm^{-3}) suggests the Goldsmid-Sharp approximation overestimates E_g. The linearly extrapolated trends from published experimental optical E_g for the EuCuSb ($E_{g,opt}\approx0.12$ eV) and $EuZn_{0.5}Sb$ ($E_{g,opt}\approx0.17$ eV for sample with $n_H\approx10^{18}$ cm^{-3}) end-members suggests a general increase in bang-gap with increasing vacancy concentration.[14,22] Interestingly, the optical measurements of the solid solution in this study suggest otherwise (Figure S10). Details and interpretations of the experimental band-gaps are found in the Optical band-gap section in the Supporting Information. Ultimately, the approximated E_g values reveal that the intrinsic charge defect ($n_i \propto e^{\frac{-E_g}{k_B T}}$) cannot account for the order of magnitude difference in n_H between $x=0$ and $x=1$ compositions. Thus the high n_H in EuCuSb is likely the result of lower defect formation energies of charged-defects.

In order to arrive at an experimental m^*_{DOS}, a single parabolic band (SPB) model within the Boltzmann transport equation framework was employed.[37] To construct an SPB model, a limiting charged carrier-scattering mechanism must be designated to describe the energy dependence of scattering. This is done by selecting a scattering parameter (λ) which defines the electron relaxation time ($\tau(\varepsilon)=\tau_0\varepsilon^{\lambda-1/2}$, $\varepsilon=\frac{E}{k_B T}$, where τ_0 is the inertial relaxation time, ε is the reduced energy, E is the energy, and T is temperature). Most commonly, the scattering mechanism is set to be acoustic deformation potential (ADP, $\lambda=0$), however, recent theoretical work suggests that polar optical scattering (POP, $\lambda=1$) is perhaps equally important in many systems.[38,39] Analysis of the μ_H vs. n_H dependence is commonly used to determine the dominant electron-scattering mechanism in a material system.[40,41] For ADP, μ_H should decrease as a function of n_H, while for POP, μ_H should increase with n_H.[42] Analysis of literature data on the $EuZn_{0.5}Sb$ system suggests that POP scattering is playing an important role in charged-carrier transport in $EuZn_{0.5}Sb$ and related materials (see Figure S7). In the current study, a plot of μ_H vs n_H also suggests POP scattering is dominant (see Figure S7b). However, n_H is not the only variable controlling μ_H in this system, meaning we cannot rely on the increasing μ_H vs n_H trend when determining the dominant mechanism of scattering—and perhaps these simplified physical models do not capture the true physics in complex semiconductors.[42] Thus, we employ both an SPS model assuming ADP dominated carrier scattering (SPB-ADP) and an SPB model assuming polar optical phonon scattering (SPB-POP) and compare the results, whilst taking the outcome with a grain of salt. Models in this work were generated using the TOSSPB script, which is an implementation of the SPB model. Details of the SPB equations used to extract m^*_{DOS}, which include the role of carrier scattering mechanisms in the SPB model, can be found the accompanying TOSSPB article published by Pöhls et al. in 2022.[43]

Figure 6d) illustrates α vs. n_H for all samples along with the SPB generated Pisarenko curves for the two end-members: EuCuSb and Eu_2ZnSb_2. The fact that the experimental data cannot be represented with a single SPB curve suggests that either m^*_{DOS} or the limiting carrier scattering mechanism may be changing. Thus Pisarenko curves were generated for every individual composition at 325 K from both SPB-ADP and SPB-POP models. From these curves we extracted the m^*_{DOS} values which are shown in Figure 6e). Regardless of the choice of ADP or POP, the m^*_{DOS} of the solid solution generally increases as a function of x. However, there is a considerable discrepancy in m^*_{DOS} depending on the selected scattering mechanism. The SPB-ADP derived m^*_{DOS} vary from 0.32–0.42 m_e with composition, while the SPB-POP derived m^*_{DOS} vary from 0.16–0.21 m_e .

This discrepancy in m^*_{DOS} highlights the importance of understanding the nature of carrier scattering and not taking τ for granted in transport models, particularly if m^*_{DOS} will be used as a metric for comparison to other materials or explaining trends in charge-transport. The differences in scattering choice becomes especially important when the SPB model is used to optimize zT, which is discussed in Figure S9. Ultimately, as the inertial effective mass (m^*_I) is

proportional to m^*_{DOS} and m^*_{DOS} decreases with added vacancies regardless of our choice in scattering mechanism, we can attribute the decrease in μ_H, at least in part, to the increase in m^*_{DOS} with x (i.e., $\mu = \frac{e\tau}{m^*_I}$). In addition to the scattering effects discussed above, there is also a possibility of magnetic carrier scattering in systems like EuCuSb and Eu_2ZnSb_2.

Composition dependent thermal properties

The total thermal conductivity (κ_{Total}) and lattice thermal conductivity (κ_L) of $EuCu_{1-x}Zn_{0.5x}Sb$ at 325 K are shown as a function of composition (x) in Figure 7a). Both κ_{Total} and κ_L decrease with increasing x, which intuitively follows from the additional scattering centers introduced as the vacancy concentration increases. The total κ falls at a faster rate than κ_L because the electrical conductivity, and thus κ_e, deceases with x. The lattice thermal conductivity of the end-members, EuCuSb ($3\,W\,mK^{-1}$) and $EuZn_{0.5}Sb$ ($0.5\,W\,mK^{-1}$), agree well with literature reports.[12,14,22] To understand the origin of the rapidly decreasing κ_L in this solid-solution series, we employ a simple kinetic gas model of lattice thermal conductivity (i.e., $\kappa_L = \frac{1}{3}C_v v^2_{avg}\tau$). The kinetic gas model allows us to decouple the effects of the mean speed of sound (v_{avg}) and the phonon relaxation time (τ) in relation to κ_L. By arriving at experimental longitudinal (v_L) and transverse (v_T) speeds of sound (Figure S12) from the elastic constants (Figure 4) and the geometric density of the samples, we can calculate an average speed of sound: $v_{avg} = \left(\frac{1}{3}\left(\frac{1}{v_L^2} + \frac{2}{v_T^2}\right)\right)^{-1/2}$.

Increasing x results in both softening of the lattice and a significant decrease in density. Thus, the impact on v_{avg} (see Figure 7b) is moderated, resulting in an overall 15 % linear decrease from $x=0$ to $x=1$. In general, changes in v_{avg} are a reasonable indicator for changes in all phonon velocities: i.e, if chemical substitutions lead to softening of the lattice and lower velocity acoustic phonons, it is reasonable to assume a similar softening of the optical phonons. Under this assumption, we can estimate the effective relaxation time, τ, as a function of x using the kinetic gas approximation. Note, we continue to assume the Dulong-Petite approximation for C_v, taking into account variations in composition. As shown in Figure 7c), the effective τ decreases by nearly an order of magnitude as x goes from 0 to 1. This suggests that phonon scattering due to disorder on the metal site and the local deviations from the ideal structure, including out-of-plane corrugation of the honeycomb lattice as evidenced by PDF, have far more impact on reducing κ_L than the softening associated with increasing x. For perspective, we can calculate a mean free path by approximating the group velocity, v_g, as the averages sound velocity v_{avg} (i.e. $l = v_{avg}\tau$, see Figure S12). While this is an underestimation of the true mean free path, since v_{avg} over-estimates v_g, we can understand that on average phonons travel four times the distance in EuCuSb than they do in $EuZn_{0.5}Sb$ before they are scattered.

A Klemens model, calculated using the TOSSPB tool,[43] in which the vacancy and Zn substitution are treated as a single averaged entity (i.e. if M_x = mass of atom x then $M_1 = M_{Cu}$ and $M_2 = \frac{M_{Zn}+M_{vac}}{2} = \frac{M_{Zn}}{2}$) provides a reasonable-fit for κ_L of the solid-solution series, upholding the central role point-defect scattering plays in this solid-solution series.[44–46] The fit is further-improved when a strain-term is introduced in the form of a radius difference (i.e. if R_x = radius of atom x then $R_1 = R_{Cu}$ and $R_2 = \frac{R_{Zn}+R_{vac}}{2} = \frac{R_{Zn}}{2}$), suggesting that while the mass contrast significantly reduces the thermal conductivity, the strain introduced by the presence of vacancies also plays a role. The latter fit is shown in Figure 7a). Details on how the Klemmens model was constructed and further analysis incorporating the new vacancy model proposed by Gurunathan et al. are presented in Figure S13.[47]

Conclusion

We demonstrated that the complete solid solution series $EuCu_{1-x}Zn_{0.5x}Sb$ from $x=0$ to $x=1$ can be synthesized using a powder-metallurgy approach, resulting in dense, single-phase samples. Surprisingly, the unit cell was found to expand in the a–b plane while contracting in the c-direction with increasing x. The unexpected expansion of the unit cell in the a–b plane with increasing vacancy concentration

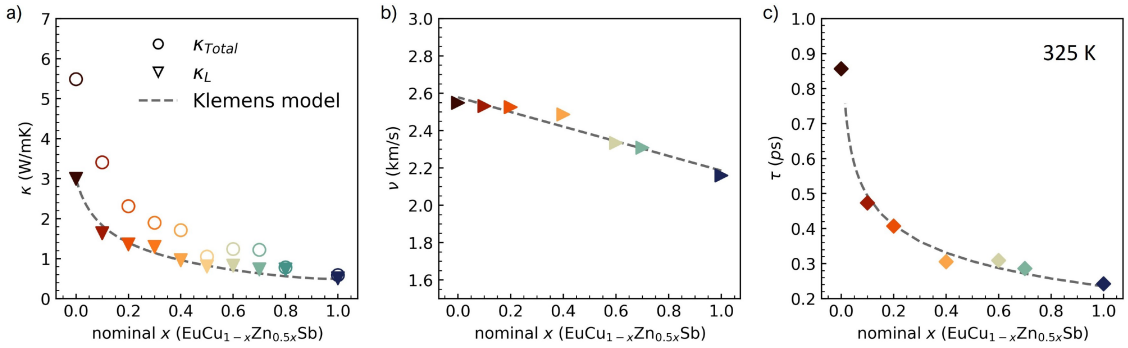

Figure 7. a) The total and lattice thermal conductivity of $EuCu_{1-x}Zn_{0.5x}Sb$ decrease with increasing vacancy concentration. The reduced κ_L is due to a combination of lattice softening, which reduces the mean phonon velocity. b) and a drastically reduced phonon mean free path (c). Note that the dashed lines in (b), (c) are shown as a guide to the eye.

suggests that anion-anion repulsion plays an important role as well. Further, the lattice parameters do not vary linearly with x, but rather, as a function of the ratio of vacant-to-filled M-sites, which implies that the vacancies, not the Cu/Zn ratio, control the average bond lengths in this solid solution. PDF analysis performed by assuming the average hexagonal ZrBeSi-structure revealed large atomic displacements on the Cu/Zn site along the c-direction, which might be consistent with locally-corrugated honeycomb M–X layers. The transition from nominally vacancy-free EuCuSb to vacancy-rich $EuZn_{0.5}Sb$ was found to cause multi-fold changes in electronic and thermal transport properties. The introduction of vacancies led to a 10-fold decrease in n_H, an increase in m_{DOS}, and an increase in E_g. Meanwhile, vacancies were found to significantly soften the lattice, therefore decreasing the phonon speed of sound. However, the most significant reduction in κ_L with increasing x was determined to be caused by the increased scattering due to vacancy-induced disorder. The vacancies were responsible for a decrease in electronic mobility, but not enough to outweigh the suppression in κ_L. Ultimately, zT is highest ($zT=0.72$) when $x=1$ ($EuZn_{0.5}Sb$), owing to the extremely low κ_L, and nearly-optimal carrier concentration.

Author Contributions

Sevan Chanakian was responsible for the bulk of the data analysis and for the Figures and text. Wanyue Peng synthesized the samples and produced the x-ray diffraction and resonant ultrasound data. Vanessa Meschke measured the electronic properties of all samples in this study. A. K. M. Ashiquzzaman Shawon performed pair-distribution function analysis and aided in data checking. Jesse Adamczyk measured the initial set of electronic properties of samples. Valeri Petkov produced the pair distribution function data. Eric Toberer helped supervise the project and provided funds. Alexandra Zevalkink is the lead supervisor of the project.

Acknowledgements

A big thank you to Prof. Katharine Page for her invaluable help teaching the authors to use the PDFgui software to conduct PDF analysis. Additionally, the authors are grateful to Prof. Rebecca Anthony and Cameron Papson for allowing us to use their FT-IR system and training us on the instrument and to Dr. Per Askland for his tremendous help collecting the SEM and EDS results included in this work. S.C.'s contributions are based upon work supported by the National Science Foundation Graduate Research Fellowship Program award No. DGE-1848739. S.C. would also like to thank funding from the Michigan Space Grant Consortium grant No. 80NSSC20M0124 V. M. acknowledges support by the National Science Foundation Graduate Research Fellowship Program award No. 1646713. A. K. M. A. S. has received funding from the National Science Foundation Award No. 2045122. V.P. contribution was funded in part by the DOE under grant No. DE-SC0021973.

Conflict of Interest

The authors declare no conflict of interest.

Data Availability Statement

The data that support the findings of this study are available from the corresponding author upon reasonable request.

Keywords: Defect Scattering · Thermoelectric Materials · Vacancies · Zintl Phases

[1] A. Cadioli, *Rend. Ist. Lomb. Accad. Sci. Lett. Parte Gen. Atti Uffic.* **2022**, *155*, 2384–9150.
[2] A. Savini, *URSI Radio Science Bulletin* **2020**, *372*, 52–55.
[3] H. S. Kim, Z. M. Gibbs, Y. Tang, H. Wang, G. J. Snyder, *APL Mater.* **2015**, *3*, 2166532X.
[4] J. Yang, L. Xi, W. Qiu, L. Wu, X. Shi, L. Chen, J. Yang, W. Zhang, C. Uher, D. J. Singh, *npj Comput. Mater.* **2016**, *2*, 15015.
[5] Z. Chen, X. Zhang, Y. Pei, *Adv. Mater.* **2018**, *30*, 15214095. <
[6] P. C. Wei, C. N. Liao, H. J. Wu, D. Yang, J. He, G. V. Biesold-McGee, S. Liang, W. T. Yen, X. Tang, J. W. Yeh, Z. Lin, J. H. He, *Adv. Mater.* **2020**, *32*, 15214095.
[7] M. T. Agne, F. R. Lange, J. P. Male, K. S. Siegert, H. Volker, C. Poltorak, A. Poitz, T. Siegrist, S. Maier, G. J. Snyder, M. Wuttig, *Matter* **2021**, *4*, 2970–2984.
[8] S. F. Matar, R. Pöttgen, *Z. Naturforsch. B* **2019**, *74*, 307–318.
[9] D. Johrendt, A. Mewis, *Z. Naturforsch. B* **1996**, *51*, 09320776.
[10] Z. Z. Zhou, K. L. Peng, H. X. Fu, H. Wu, G. Y. Wang, X. Y. Zhou, *Phys. Rev. Appl.* **2021**, *16*, 23317019.
[11] Z. Zhou, K. Peng, S. Xiao, Y. Wei, Q. Dai, X. Lu, G. Wang, X. Zhou, *J. Phys. Chem. Lett.* **2022**, *13*, 19487185.
[12] S. Chanakian, D. Uhl, D. Neff, F. Drymiotis, J. Park, V. Petkov, A. Zevalkink, S. Bux, *J. Mater. Chem. A* **2020**, *8*, 6004–6012.
[13] T. Sekimoto, K. Kurosaki, H. Muta, S. Yamanaka, *Appl. Phys. Lett.* **2006**, *89*, 092108.
[14] W. Zhang, C. Chen, H. Yao, W. Xue, S. Li, F. Bai, Y. Huang, X. Li, X. Lin, F. Cao, J. Sui, S. Wang, B. Yu, Y. Wang, X. Liu, Q. Zhang, *Chem. Mater.* **2020**, *32*, 6983–6989.
[15] Z. Feng, Y. Fu, Y. Yan, Y. Zhang, D. J. Singh, *Phys. Rev. B* **2021**, *103*, 224101.
[16] S. F. Wang, Z. G. Zhang, B. T. Wang, J. R. Zhang, F. W. Wang, *Chin. Phys. Lett.* **2021**, *38*, 046301.
[17] Y. Huang, C. Chen, W. Zhang, X. Li, W. Xue, X. Wang, Y. Liu, H. Yao, Z. Zhang, Y. Chen, F. Cao, X. Liu, Y. Wang, Q. Zhang, *Sci. China Mater.* **2021**, *64*, 2541–2550.
[18] E. Haque, *RSC Adv.* **2021**, *11*, 15486–15496.
[19] D. K. Wilson, B. Saparov, S. Bobev, *Z. Anorg. Allg. Chem.* **2011**, *637*, 2018–2025.
[20] H. Ma, G. Li, X. Zhang, H. Huang, B. Duan, P. Zhai, *J. Alloys Compd.* **2020**, *843*, 155981.
[21] C. Chen, Z. Feng, H. Yao, F. Cao, B. H. Lei, Y. Wang, Y. Chen, D. J. Singh, Q. Zhang, *Nat. Commun.* **2021**, *12*, 5718.
[22] C. Chen, W. Xue, S. Li, Z. Zhang, X. Li, X. Wang, Y. Liu, J. Sui, X. Liu, F. Cao, Z. Ren, C. W. Chu, Y. Wang, Q. Zhang, *Proc. Natl. Acad. Sci. USA* **2019**, *116*, 2831–2836.

[23] C. Chen, X. Li, W. Xue, F. Bai, Y. Huang, H. Yao, S. Li, Z. Zhang, X. Wang, J. Sui, X. Liu, F. Cao, Y. Wang, Q. Zhang, *Nano Energy* **2020**, *73*, 104771.
[24] H. Yao, C. Chen, W. Xue, F. Bai, F. Cao, Y. Lan, X. Liu, Y. Wang, D. J. Singh, X. Lin, Q. Zhang, *Sci. Adv.* **2021**, *7*, eabd6162.
[25] J. Zhang, X. Liu, Q. Liu, S. Xia, *J. Alloys Compd.* **2020**, *816*, 152508.
[26] H. Takahashi, K. Aono, Y. Nambu, R. Kiyanagi, T. Nomoto, M. Sakano, K. Ishizaka, R. Arita, S. Ishiwata, *Phys. Rev. B* **2020**, *102*, 174425.
[27] T. Mishra, I. Schellenberg, M. Eul, R. Pöttgen, *Z. Kristallogr.* **2011**, *226*, 590–601.
[28] D. A. Freedman, D. Roundy, T. A. Arias, *Phys. Rev. B* **2009**, *80*, 064108.
[29] D. C. Fredrickson, *J. Am. Chem. Soc.* **2012**, *134*, 5991–5999.
[30] X. Wang, S. Ramírez-Hinestrosa, J. Dobnikar, D. Frenkel, *Phys. Chem. Chem. Phys.* **2020**, *22*, 10624–10633.
[31] A. Jain, S. P. Ong, G. Hautier, W. Chen, W. D. Richards, S. Dacek, S. Cholia, D. Gunter, D. Skinner, G. Ceder, K. A. Persson, *APL Mater.* **2013**, *1*, 011002.
[32] G. R. Somayajulu, *J. Chem. Phys.* **1958**, *28*, 814–821.
[33] J. Emmerlich, D. Music, A. Houben, R. Dronskowski, J. M. Schneider, *Phys. Rev. B* **2007**, *76*, 224111.
[34] E. Isotta, W. Peng, A. Balodhi, A. Zevalkink, *Angew. Chem. Int. Ed.* **2023**, *62*, e202213649.
[35] T. M. Tritt, *Thermal Conductivity: Theory, properties and applications, Vol. 53*, Kluwer Academic/Plenum Publishers, New York, **2004**.
[36] H. J. Goldsmid, J. W. Sharp, *J. Electron. Mater.* **1999**, *28*, 869–872.
[37] S. D. Kang, G. Jeffrey Snyder, Transport property analysis method for thermoelectric materials: Material quality factor and the effective mass model, in *Advances in Thermoelectricity: Foundational Issues*, *Materials and Nanotechnology* **2021**.
[38] A. M. Ganose, J. Park, A. Faghaninia, R. Woods-Robinson, K. A. Persson, A. Jain, *Nat. Commun.* **2021**, *12*, 2222.
[39] J. H. Pöhls, S. Chanakian, J. Park, A. M. Ganose, A. Dunn, N. Friesen, A. Bhattacharya, B. Hogan, S. Bux, A. Jain, A. Mar, A. Zevalkink, *Mater. Horiz.* **2021**, *8*, 209–215.
[40] K. Seeger, *Semiconductor Physics*, Springer Vienna, Vienna, **1973**.
[41] J. Cao, J. D. Querales-Flores, A. R. Murphy, S. Fahy, I. Savić, *Phys. Rev. B* **2018**, *98*, 205202.
[42] A. M. Ganose, J. Park, A. Jain, *arXiv*:2210.01746 [cond-mat.mtrl-sci] **2022**.
[43] J. H. Pöhls, Y. Mozharivskyj, *Comput. Mater. Sci.* **2022**, *206*, 111152.
[44] P. G. Klemens, *Phys. Rev.* **1960**, *119*, 507.
[45] J. Callaway, H. C. von Bayer, *Phys. Rev.* **1960**, *120*, 1149 .
[46] B. Abeles, *Phys. Rev.* **1963**, *131*, 1906.
[47] R. Gurunathan, R. Hanus, M. Dylla, A. Katre, G. J. Snyder, *Phys. Rev. Appl.* **2020**, *13*, 034011.
[48] V. Petkov, *J. Appl. Crystallogr.* **1989**, *22*, 387–389.
[49] C. L. Farrow, P. Juhas, J. W. Liu, D. Bryndin, E. S. Boin, J. Bloch, T. Proffen, S. J. Billinge, *J. Phys. Condens. Matter* **2007**, *19*, 335219.
[50] K. Momma, F. Izumi, *J. Appl. Crystallogr.* **2008**, *41*, 653–658.
[51] R. G. Leisure, F. A. Willis, *J. Phys. Condens. Matter* **1997**, *9*, 6001.
[52] R. G. Leisure, *Ultrasonic Spectroscopy*, Cambridge University Press, Cambridge, **2017**.
[53] F. F. Balakirev, S. M. Ennaceur, R. J. Migliori, B. Maiorov, A. Migliori, *Rev. Sci. Instrum.* **2019**, *90*, 121401.
[54] K. A. Borup, E. S. Toberer, L. D. Zoltan, G. Nakatsukasa, M. Errico, J. P. Fleurial, B. B. Iversen, G. J. Snyder, *Rev. Sci. Instrum.* **2012**, *83*, 123902.
[55] S. Iwanaga, E. S. Toberer, A. Lalonde, G. J. Snyder, *Rev. Sci. Instrum.* **2011**, *82*, 063905.
[56] N. Sangiorgi, L. Aversa, R. Tatti, R. Verucchi, A. Sanson, *Opt. Mater.* **2017**, *64*, 18–25.
[57] P. Makuła, M. Pacia, W. Macyk, *J. Phys. Chem. Lett.* **2018**, *9*, 6814–6817.

Manuscript received: January 23, 2023
Accepted manuscript online: May 4, 2023
Version of record online: May 4, 2023

Research Articles

Thermoelectric Materials

S. Chanakian, W. Peng, V. Meschke, A. K. M. Ashiquzzaman Shawon, J. Adamczyk, V. Petkov, E. Toberer, A. Zevalkink* ——— **e202301176**

Investigating the Role of Vacancies on the Thermoelectric Properties of EuCuSb-Eu_2ZnSb_2 Alloys

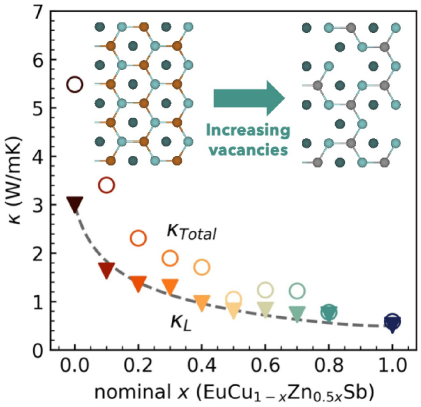

In this work, we investigate the impact of vacancies on the thermoelectric properties of the EuCuSb-$EuZn_{0.5}Sb$ solid solution. Vacancies in the planar honeycomb lattice cause a decrease in sound velocity and a sharp increase in point defect scattering, which combine to yield an 80% decrease in lattice thermal conductivity. Ultimately, the maximum *zT* increases from 0.09 to 0.7 as the composition varies from EuCuSb to $EuZn_{0.5}Sb$.